Fermi National Accelerator Laboratory

FERMILAB-Conf-90/118-E
[E-741/CDF]

Recent Results on Direct Photons from CDF *

The CDF Collaboration

presented by

Robert M. Harris
Fermi National Accelerator Laboratory
P.O. Box 500
Batavia, Illinois 60510

June 1, 1990

---

* To be published in the prodceedings of the Workshop on Hadron Structure Functions and Parton Distributions, Batavia, Illinois, April 26-28, 1990.

Operated by Universities Research Association Inc. under contract with the United States Department of Energy

CDF/PUB/JET/PUBLIC/1210
Fermilab-Conf-90/118-E
To be published in the Proceedings of
the Workshop on Hadron Structure Functions
and Parton Distributions, Fermi National
Accelerator Laboratory, April 26-28, 1990

Recent Results on Direct Photons from CDF

The CDF Collaboration[*]
Presented by Robert M. Harris
Fermi National Accelerator Laboratory
Batavia, IL 60510, USA

June 1, 1990

Abstract

We report on preliminary measurements of direct photons in $\bar{p}p$ collisions at $\sqrt{s} = 1.8$ TeV from the 1988-89 run of the Collider Detector at Fermilab (CDF). The inclusive direct photon cross section, measured for photon transverse momentum in the range $13 < P_t < 68$ GeV, has an excess at low P_t compared to recent Quantum Chromodynamic (QCD) calculations. The pseudorapidity distribution of the away-side jet, for events with $27 < P_t < 33$ GeV, agrees with QCD predictions. Measurements of the K_t kick in photon-jet events are also presented.

1 Physics Motivation

Measurements of photons, coming directly from the hard collision of partons, provide a test of QCD which is free from the energy measurement uncertainties associated with jets. The compton diagrams, shown in Fig. 1a, dominate the production of direct photons at the Born level, so measurements of direct photons are sensitive to the gluon distribution of the proton. The high center of mass energy of the Tevatron allows the CDF detector[1] to test QCD and probe the gluon distribution in a previously unexplored range of fractional momentum ($.015 < x < .075$).

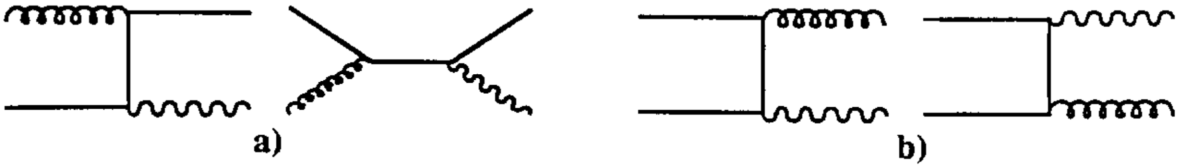

Figure 1: Lowest order diagrams for direct photons. a) Compton and b) annihilation.

---

[*] The collaborating institutions are listed in Appendix A

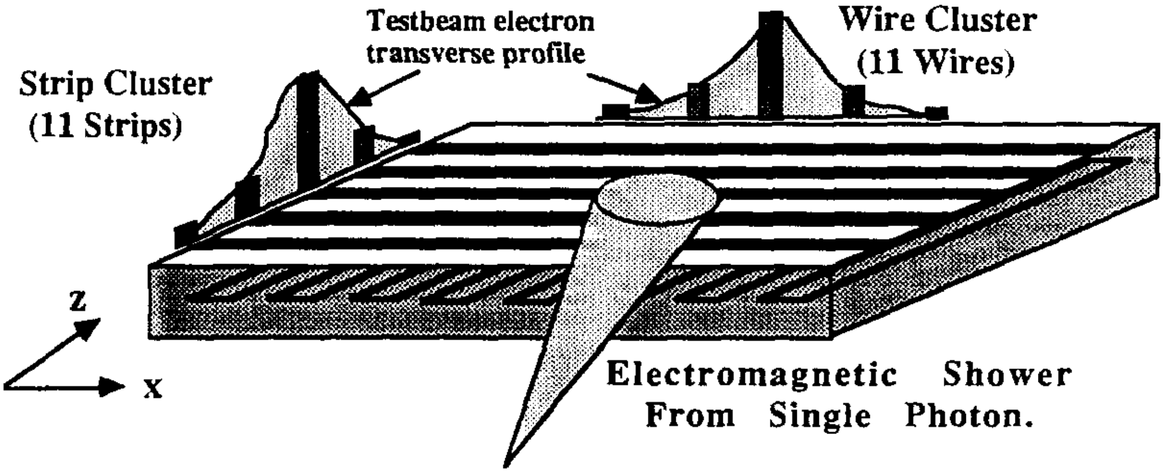

Figure 2: The transverse profile of a photon in a CES chamber.

2 Direct Photon-Background Separation

The signal for a direct photon is the deposition of isolated energy in the electromagnetic calorimeter with no associated charged track in the tracking chamber. The dominant background comes from the decays of the neutral mesons π^0 and η into multiple photons. We employ two methods for separating direct photons from neutral mesons: method I uses the transverse profile of the electromagnetic shower and method II counts the number of conversion pairs produced just outside the tracking chamber.

2.1 Method I: Transverse Shower Profiles

The central electromagnetic strip (CES) chambers[2] are multiwire proportional chambers embedded in the central electromagnetic calorimeter at shower maximum (6 radiation lengths). A calorimeter cluster consists of three projective towers spanning $\Delta\eta \times \Delta\phi \approx .3 \times .26$. The CES anode wires are perpendicular to cathode strips, as shown in Fig. 2. Within the boundaries of the calorimeter cluster are CES strip and wire clusters, consisting of eleven strips and eleven wires respectively. The highest energy strip cluster and the highest energy wire cluster are chosen to measure the transverse profile and position of photons. The electromagnetic shower from a single photon, shown schematically in Fig. 2, has a narrow transverse profile, and produced a small χ^2 when fit to an electron transverse profile. Conversely, a neutral meson decaying into multiple photons has a wider profile, and produced a larger χ^2 when fit to an electron transverse profile. Fits were done for both the wire and strip clusters and each raw χ^2 was scaled by a function of the calorimeter cluster energy to produce a corrected χ^2 which was independent of energy for electrons and (presumably) photons. Then the *average* χ^2 ((strip χ^2 + wire χ^2)/2) was the variable used to separate

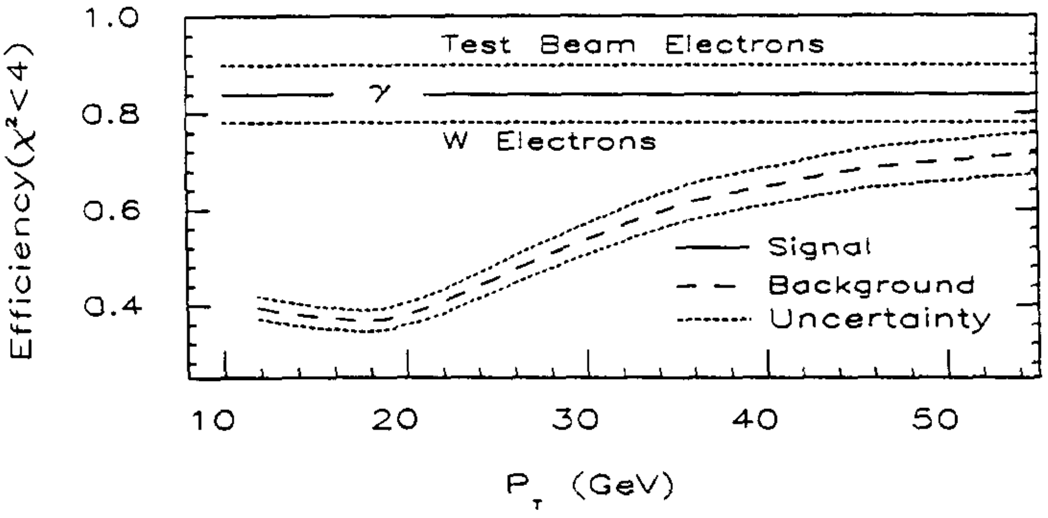

Figure 3: The efficiency for photons and background to have $\chi^2 < 4$ vs. P_t

single photons from neutral mesons.

Let ϵ_γ be the efficiency for a single photon to have $\chi^2 < 4$, and let ϵ_{π^0} be the efficiency for multiple photons from neutral meson decays to have $\chi^2 < 4$. Then the number of clusters with $\chi^2 < 4$ and $\chi^2 > 4$ is related to the number of photons and neutral mesons by:

$$\begin{bmatrix} N_{\chi^2<4} \\ N_{\chi^2>4} \end{bmatrix} = \begin{bmatrix} \epsilon_\gamma & \epsilon_{\pi^0} \\ 1-\epsilon_\gamma & 1-\epsilon_{\pi^0} \end{bmatrix} \begin{bmatrix} N_\gamma \\ N_{\pi^0} \end{bmatrix} \tag{1}$$

Inverting Eq. 1 gives the number of photons and neutral mesons:

$$\begin{bmatrix} N_\gamma \\ N_{\pi^0} \end{bmatrix} = \frac{1}{\epsilon_\gamma - \epsilon_{\pi^0}} \begin{bmatrix} 1-\epsilon_{\pi^0} & -\epsilon_{\pi^0} \\ \epsilon_\gamma - 1 & \epsilon_\gamma \end{bmatrix} \begin{bmatrix} N_{\chi^2<4} \\ N_{\chi^2>4} \end{bmatrix} \tag{2}$$

We estimated ϵ_γ using a measured testbeam electron shower for each photon in a full detector simulation which includes all analysis cuts (see section 2.1.1). Figure 3 shows the estimated photon χ^2 efficiency midway between the upper systematic bound from raw testbeam electrons and the lower systematic bound from W electrons. Similarly, we estimated ϵ_{π^0} from the simulated decays of the neutral mesons π^0, η, and K_s^0. Figure 3 shows the P_t dependence of the χ^2 efficiency of this background. Here we assumed the mesons π^0, η, and K_s^0 are produced with relative rates 1 : 0.6 : 0.25. Varying the relative meson production rates within the limits 1 : 0.75 : 0.5 and 1 : 0.45 : 0.0 produced only a small variation in efficiency. The largest systematic uncertainty on the background χ^2 efficiency, coming from the propagation of the photon simulation uncertainty, is displayed in Fig. 3. This is the dominant systematic uncertainty in the measurement of the direct photon cross section using method I. At high P_t the multiple photons from a neutral meson are so close together that the

Trigger Cuts	**γ Acceptance**
$P_t > 10$ GeV (77.5 nb^{-1})	~1 at 14 GeV
$P_t > 23$ GeV (2.55 pb^{-1})	~1 at 27 GeV
$E_{T,HAD}/E_{T,EM} < .125$	~1
Isolation: $E_{CONE}/E_\gamma < .15$	.82 → .96
Analysis Cuts	
No Track Pointing at Photon	.98
2nd CES Strip and Wire Clusters < 1 GeV	.86
CES Strip and Average $\chi^2 < 20$	~1
14 cm < |CES Z| < 217 cm	.92
|CES X| < 17.5 cm	.77
$\|\eta\| < 0.9$	~1
|Z Vertex| < 50 cm ($\sigma_Z = 32$ cm)	.88
Missing E_t Significance < 3	~1
	.43 → .50

Table 1: The data sample, trigger, and analysis cuts for method I

χ^2 efficiency for the background is almost the same as for a single photon. Thus, for high values of P_t, Eq. 2 becomes singular and so does the systematic uncertainty in the number of direct photons. To avoid large systematic uncertainties, method I was only used up to transverse momenta of 33 GeV.

2.1.1 Data Sample and Event Selection for Method I

The data sample, trigger, and cuts for the method I analysis are summarized in table 1. The low P_t trigger was prescaled to reduce the rate throughout the run, while the high P_t trigger was not prescaled. The triggers required that 89% of the transverse energy of the photon be in the electromagnetic compartment of the calorimeter and also required the photon to be *isolated*: the extra energy inside a cone of radius $\sqrt{(\Delta\eta)^2 + (\Delta\phi)^2} = 0.7$ centered on the photon is required to be less than 15% of the photon energy. Charged background is eliminated by requiring there be no track pointing at the calorimeter cluster associated with the photon. Neutral hadron background is reduced by requiring that additional strip chamber clusters within the boundaries of the calorimeter cluster be less than 1 GeV each. Fiducial cuts are imposed to avoid uninstrumented regions at the strip chamber edges, and a cut on the z coordinate of the event vertex was imposed to maintain the calorimeter towers projective geometry. Finally, a cut on the event missing transverse energy significance ($\sqrt{(\Sigma\vec{E}_x)^2 + (\Sigma\vec{E}_y)^2}/\sqrt{\Sigma E_t}$) removes residual cosmic ray *bremsstrahlung*. The cuts have an acceptance ranging from 43% (at 14 GeV) to 50% (at 33 GeV). The P_t depen-

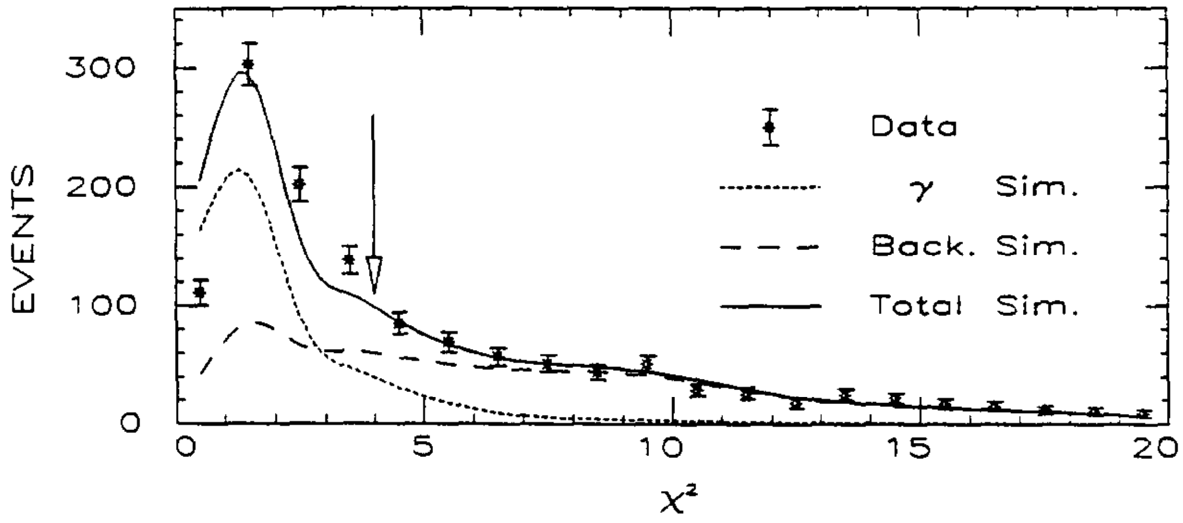

Figure 4: The χ^2 distribution for the data compared to simulation.

dence of the acceptance comes from the fractional isolation cut which eliminates more photon events at low P_t because of fluctuations in the underlying event.

The χ^2 distribution of the data after all cuts is shown in fig. 4 for the interval $14 < P_t < 20$ GeV. The peak at low χ^2 is produced predominantly by direct photons. The background and photon simulations have been normalized to the number of events using Eq. 2. For $\chi^2 > 4$ the simulation models the data quite well. For $\chi^2 < 4$ the simulated distribution has lower χ^2 than the data. Similarly, testbeam electrons have a lower χ^2 than electrons from the decay $W \rightarrow e\nu$, which gave the systematic bounds in χ^2 efficiency shown previously in Fig. 3. Only the efficiency for $\chi^2 < 4$ is needed in the method I technique of Eq. 2; knowledge of the detailed shape of the χ^2 distribution inside of $\chi^2 < 4$ is not necessary.

2.1.2 Results from Method I

Using the number of direct photons (N_γ) in a bin of transverse momentum (ΔP_t) and a bin of pseudorapidity ($\Delta\eta$), the acceptance (α) and the integrated luminosity ($\int L$), we obtain the inclusive direct photon cross section:

$$\frac{d^2\sigma}{dP_t d\eta} = \frac{N_\gamma}{\Delta P_t \cdot \Delta\eta \cdot \alpha \cdot \int L} \tag{3}$$

which is shown twice in Fig. 5. The inner error bars are the statistical uncertainty and the outer error bars are the P_t dependent part of the systematic uncertainty combined in quadrature with the statistical uncertainty. The P_t independent component of the systematic uncertainty is shown as the normalization uncertainty. In Fig. 5 our measurement is compared to QCD calculations[3] using three different sets of parton distribution functions[4,5] for a single choice of the renormalization scale $Q^2 = P_t^2$.

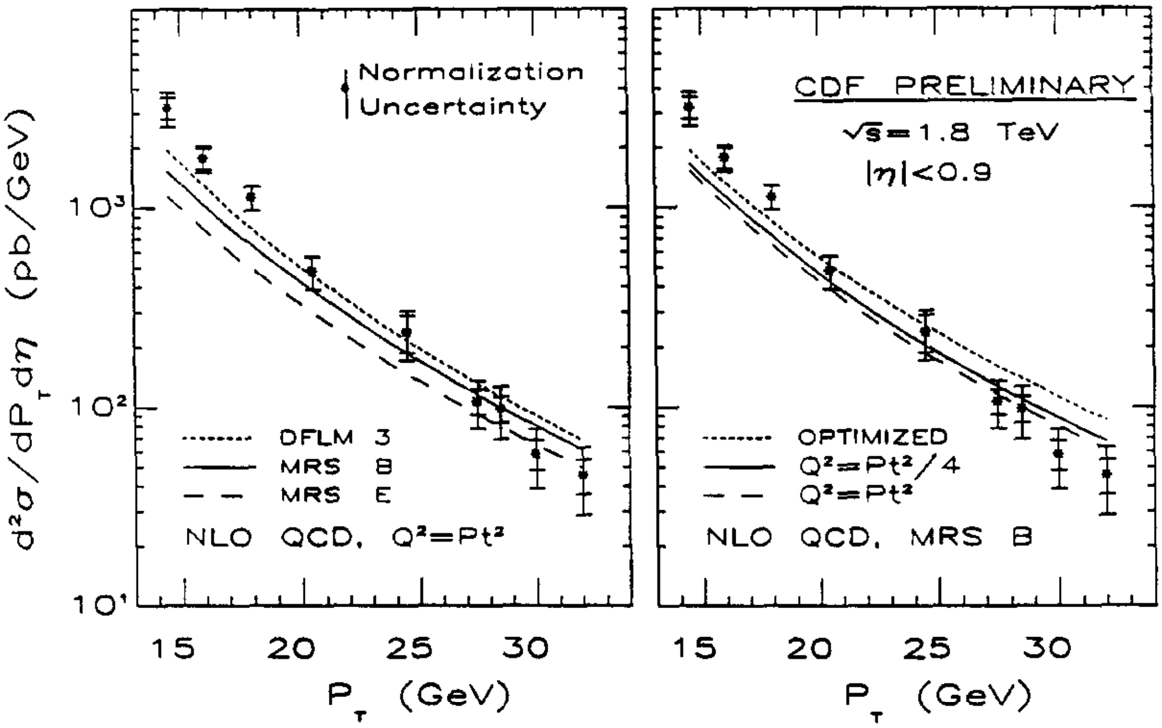

Figure 5: The inclusive direct photon cross section from method I and QCD predictions.

Also in Fig. 5, the same measurement is compared to QCD calculations[3] using three different choices of the renormalization scale for a single set of parton distribution functions[5]. The calculations are discussed in greater detail in section 3. The cross section measured with method I has a slightly steeper dependence on P_t than the QCD predictions.

2.2 Method II: Photon Conversions

The central drift tubes[6] (CDT) are three layers of gas counters just outside the central tracking chamber (CTC), as shown in Fig. 6a. The outer wall of the CTC and the inner two CDT layers provide 18% of a radiation length for the conversion of photons into electron-positron pairs. Neutral mesons decaying into two photons are twice as likely to produce a conversion pair, which is then detected as a CDT *hit* cluster. Requiring $\chi^2 < 4$ reduced the neutral meson background and preferentially selected asymmetric decays. Conversions of direct photons, or conversions of the higher energy photon from an asymmetric decay, produced no azimuthal separation of the CDT hits and CES clusters, and made the spike at zero in Fig. 6b. However, conversions of the lower energy photon of an asymmetric decay produced a measurable azimuthal separation of CDT hits and CES clusters, and made the bump shown in Fig. 6b. From this plot the production ratio γ/π^0 was estimated.

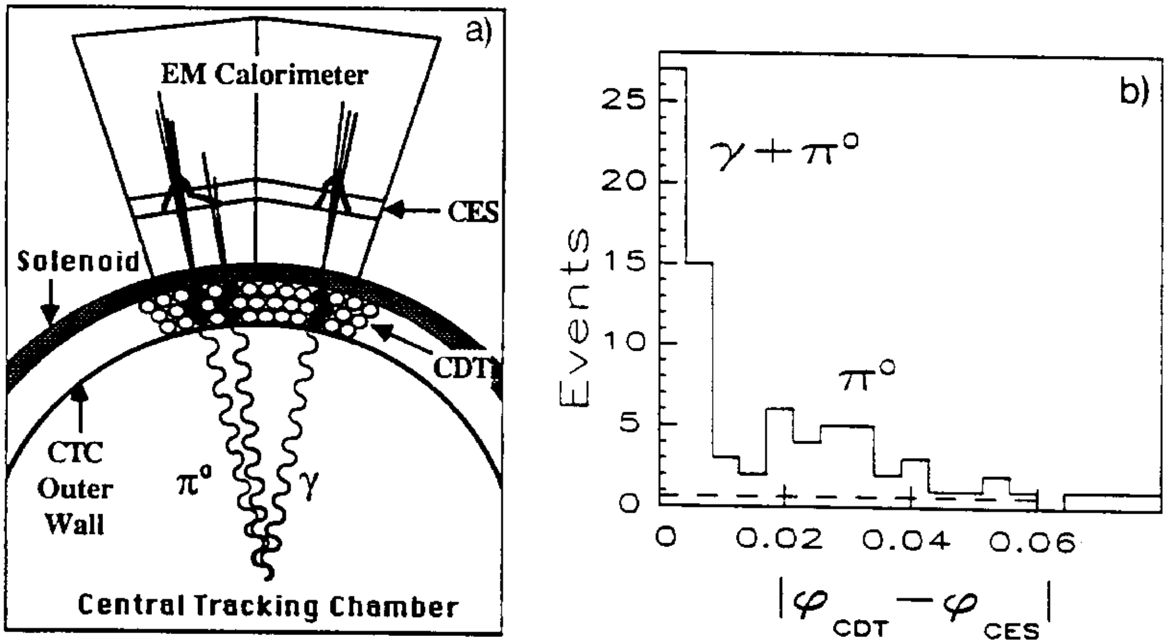

Figure 6: **a)** Conversions detected in the CDT and associated CES cluster. **b)** Azimuthal separation of CDT and CES clusters for $9 < P_t < 11$ GeV.

From the γ/π^0 ratio, and the number of neutral clusters in the calorimeter (N_C), and the total number of CDT hits ($N_{H,total}$) associated with neutral clusters, we estimated the probability of observing a conversion:

$$P_\gamma = \frac{N_{H,total}}{N_C}\left[\frac{1+\gamma/\pi^0}{2+\gamma/\pi^0}\right] \approx 0.10 \pm 0.02 \tag{4}$$

The conversion probability expected from the amount of material and the efficiency of hit selection is about 11%, consistent with the value given in Eq. 4 within the systematic uncertainty. This systematic uncertainty, which is approximately P_t independent, dominated the uncertainty in the normalization of the direct photon cross section from method II. Finally, the number of clusters with one or more hit (N_H) is related to the number of photons and neutral mesons by:

$$\begin{bmatrix} N_H \\ N_C \end{bmatrix} = \begin{bmatrix} P_\gamma & 2P_\gamma - P_\gamma^2 \\ 1 & 1 \end{bmatrix} \begin{bmatrix} N_\gamma \\ N_{\pi^0} \end{bmatrix} \tag{5}$$

Inverting Eq. 5 gives the number of photons and background:

$$\begin{bmatrix} N_\gamma \\ N_{\pi^0} \end{bmatrix} = \frac{1}{P_\gamma^2 - P_\gamma} \begin{bmatrix} 1 & P_\gamma^2 - 2P_\gamma \\ -1 & P_\gamma \end{bmatrix} \begin{bmatrix} N_H \\ N_C \end{bmatrix} \tag{6}$$

2.2.1 Data Sample and Event Selection for Method II

The data sample for the method II analysis came from the trigger discussed in section 2.1.1, except the integrated luminosity was 45 nb^{-1} and 1.4 pb^{-1} for the low and high P_t thresholds respectively. The analysis cuts in section 2.1.1 were used except: the CES χ^2 cuts were not present, the CES 2nd cluster cut was at 2 GeV with a corresponding γ acceptance of 90%, and there was a CES strip and wire energy matching cut with a γ acceptance of 91%. In addition, the following cuts were introduced for the method II analysis:

- CES average $\chi^2 < 4$ to reduce the neutral meson background.
- CDT-CES $\Delta\phi < 0.1(0.07)$ for the low (high) P_t trigger.
- CDT-CES $\Delta z < 10$ cm to reduce stray track backgrounds.

The $\Delta\phi$ and Δz cuts, used in the definition of a CDT hit, had an efficiency of 100% and 75% respectively. These efficiencies are part of the observed photon conversion probability defined in Eq. 4. Background CDT hits caused by stray tracks were estimated from CDT-CES $\Delta\phi$ distributions, and were subtracted from N_H before Eq. 6 was used to find N_γ. A typical amount of random background is illustrated by the dashed line in Fig. 6b. The total direct photon acceptance was between 35% and 42% depending on P_t. Finally, the number of photons, acceptance, and integrated luminosity were used in Eq. 3 to determine the inclusive direct photon cross section from method II.

3 Inclusive Direct Photon Cross Section

The inclusive direct photon cross sections, measured separately with method I and method II, are each shown twice in Fig. 7 along with the same QCD calculations[3] that were presented in Fig. 5. The error bars on the method II points are statistical uncertainties. The outer error bars on the method I points are the statistical uncertainties and the P_t dependent component of the systematic uncertainties added in quadrature. The P_t independent component of the systematic uncertainty for each method is shown separately as the normalization uncertainty. The cross sections measured with the two methods agree within errors. The method II analysis extends to higher P_t than the more precise method I analysis. We conclude that the measured cross section has an excess at low P_t compared to the QCD predictions shown; at $P_t > 20$ GeV the measured cross section agrees with the QCD predictions.

Before drawing conclusions about the behavior of the gluon distribution at low x, the reader should consider the uncertainties in the QCD calculation. The QCD calculations approximate the experimental *isolation* cut, requiring that partons inside a cone of radius 0.7 around the photon have less than 15% of the photon energy. The

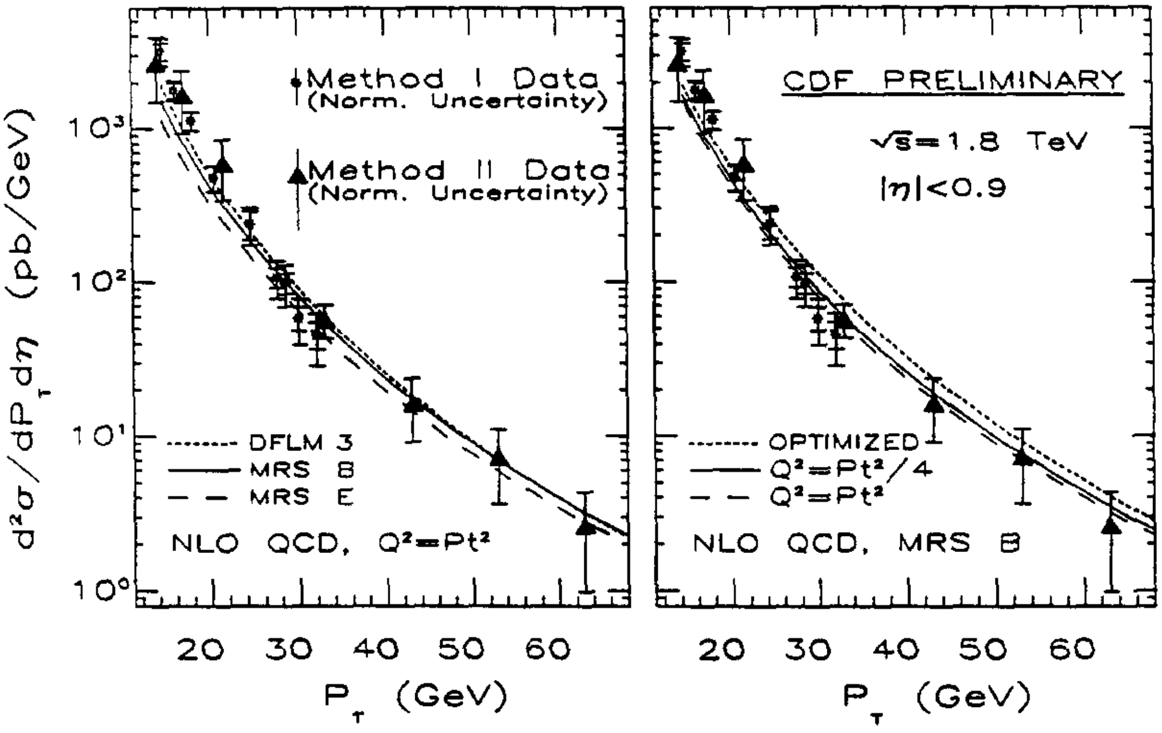

Figure 7: The inclusive direct photon cross section from method I and method II compared to QCD predictions.

calculated cross section decreases by less than 5% when the isolation condition is tightened to allow no partons in the isolation cone, and it increases by less than 7% when the isolation condition is loosened by requiring a smaller cone of radius 0.4 for the same 15% energy cut. The uncertainties in the QCD calculation associated with truncating the perturbation expansion can be roughly estimated by varying the choice of renormalization scale. The calculations presented in Fig. 5 and Fig. 7 have equal renormalization scales and factorization scales, labeled by Q^2, except for the calculation labeled *optimized* which has a renormalization scale $\mu_R^2 \approx P_t^2/50$ and a factorization scale $\mu_F^2 \approx 50P_t^2$. The calculations are at next to leading order, that is they include all diagrams of order $\alpha\alpha_s^2$, except for final state photon *bremsstrahlung* (see Fig. 8) which is included only at an effective order of $\alpha\alpha_s$. Photon *bremsstrahlung* contributes significantly to the cross section at low P_t, and is calculated by convolving leading order diagrams with the *effective fragmentation function* for obtaining photons from partons. The effective fragmentation function of a parton into a photon has never been measured. It is modeled by a QED splitting function evolved to account for emission of soft and collinear gluons.

Considering the current uncertainties on the theoretical calculation and the preliminary nature of our measurement, it may be premature to draw conclusions about

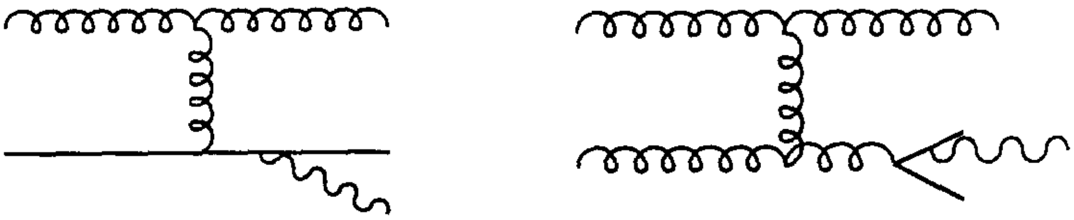

Figure 8: Examples of *bremsstrahlung* diagrams for direct photon production.

the detailed shape of the gluon distribution from Fig. 5 or Fig. 7.

4 Leading Jet in Photon Events

Direct photons are produced along with a quark or gluon which appears in the CDF detector as a jet of hadrons. From the distribution of the jet, in both polar and azimuthal angles, we can obtain additional information about the hard scattering of partons. We find jets using a fixed cone clustering algorithm[7] with radius $\sqrt{(\Delta\eta)^2 + (\Delta\phi)^2} = 0.7$. The leading jet in a direct photon event is the jet with the highest transverse momentum[7]. We measure photons and neutral mesons for $|\eta| < 0.9$ and jets for $|\eta_j| < 3.2$. For the following measurements the data sample came from the trigger discussed in section 2.1.1, except the integrated luminosity was 67 nb^{-1} and 1.4 pb^{-1} for the low and high P_t thresholds respectively. The method I analysis cuts in section 2.1.1 were used, with a few exceptions noted in section 2.2.1, and the CES average χ^2 was required to be less than 25.

4.1 Leading Jet Pseudorapidity Distribution

Pseudorapidity is related to polar angle by $\eta = \ln(\cot(\theta/2))$. The pseudorapidity of the leading jet has a distribution which depends on the convolution of parton momentum distributions, hard scattering angular distributions, and the $1/\hat{s}^2$ dependence of the parton subprocess cross section. Thus, measurements of the leading jet pseudorapidity distribution can be used to study parton momentum distributions and angular distributions for two different final states: photon-parton final states for the photon signal and parton-parton final states for the photon background.

In Fig. 9 the pseudorapidity distribution of the leading jet is shown separately for photons and neutral mesons with $27 < P_t < 33$ GeV. The error bars on the points are statistical errors only; the systematic uncertainty for photons is roughly ±40%. The leading jet pseudorapidity distribution for photons (labeled γ-jet) is compared to a full next to leading order calculation[8] and a leading order calculation. The former calculation's normalization is absolute, but the latter calculation was multiplied by 1.37 to fit the data at low $|\eta_j|$. Within statistics the data is compatible with either calculation. The leading jet pseudorapidity distribution for the background (labeled π^0-jet) is compared to a leading order QCD calculation of parton-parton scattering,

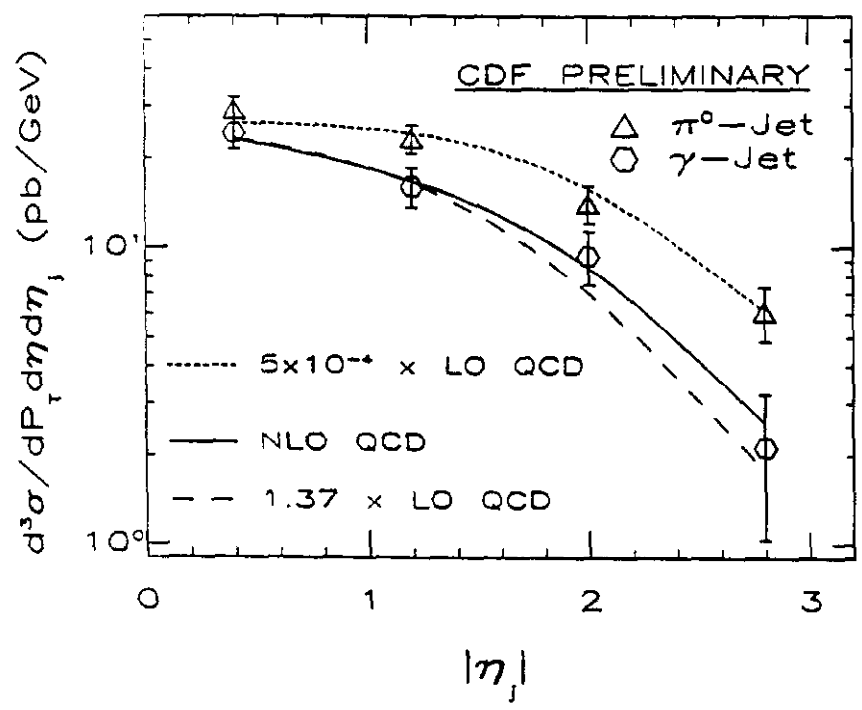

Figure 9: The pseudorapidity distribution of the leading jet, for photon and background events, is compared to QCD predictions (see text).

without fragmentation of the final state partons. This calculation was multiplied by 5×10^{-4} to fit the measured data (this number can be interpreted as an order of magnitude estimate of the probability for a gluon to fragment into a single isolated neutral meson). Measurement of the leading jet pseudorapidity in events with lower photon P_t are more difficult because of fluctuations in the underlying event, and these distributions are still being studied.

4.2 K_t kick in photon events

In lowest order QCD the jet and photon have equal and opposite transverse momentum. We have used $\Delta\phi$, the azimuthal angle between the photon and the leading jet in the transverse plane, to measure how much real events deviate from the lowest order picture. As shown in Fig. 10a, we only use the leading jet to measure $\Delta\phi$, and redefine the magnitude of the transverse momentum of the leading jet to be equal to the transverse momentum of the photon. Then the vector sum of the transverse momentum of the photon and the leading jet must lie along the perpendicular bisector of $\Delta\phi$ in the transverse plane. The magnitude of this vector

$$K_{t\perp} = 2P_t \cos\frac{\Delta\phi}{2} \tag{7}$$

is always zero for lowest order QCD calculations in the naive parton model. Since higher order effects will cause $\vec{K}_{t\perp}$ to deviate from zero, an interesting variable is the

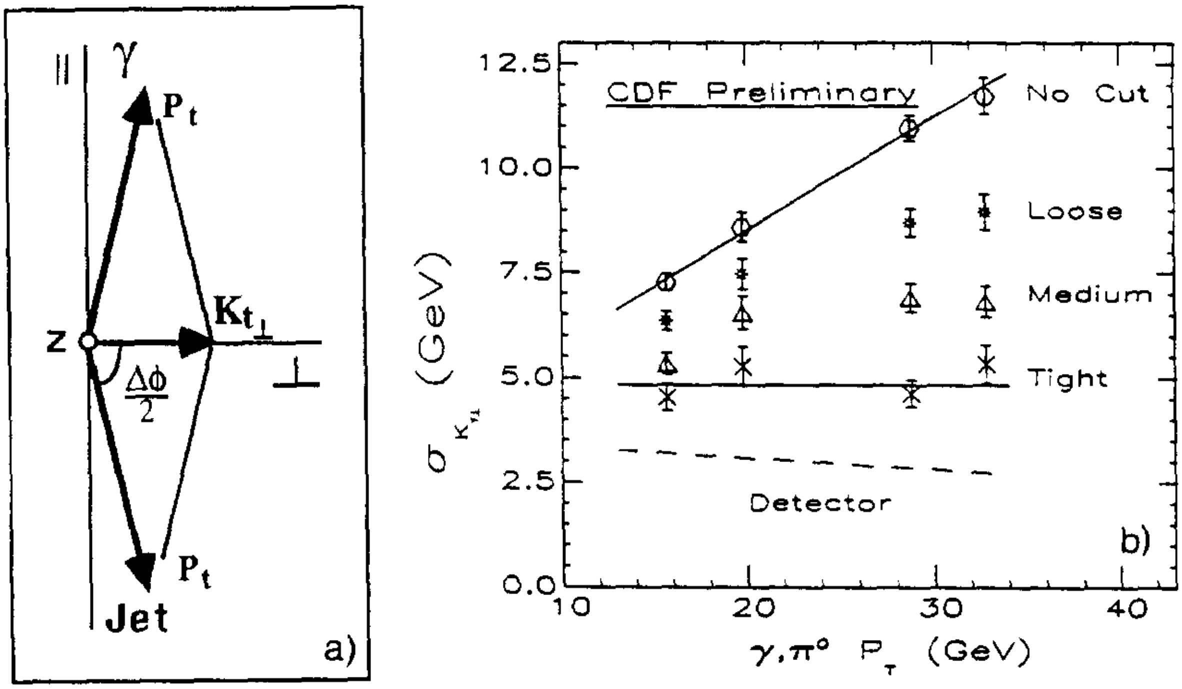

Figure 10: a) Definition of measured K_t kick. b) The RMS deviation of the K_t kick from zero vs. the photon (with background) P_t.

RMS deviation of $\vec{K_{t\perp}}$ about zero:

$$\sigma_{K_{t\perp}} = \sqrt{\langle K_{t\perp}^2 \rangle} \tag{8}$$

In Fig. 10b we show some measurements of the RMS deviation of $\vec{K_{t\perp}}$ about zero, for direct photons with background (we have not done a background subtraction). The events in this plot were required to have a leading jet with greater than 10 GeV transverse momentum and $\Delta\phi > 90°$. With no additional cuts, the hexagons show that the RMS deviation of the K_t kick increases with increasing photon (and background) P_t, and we fit it with a solid line to guide the eye. The magnitude of this K_t kick is a significant deviation from the lowest order QCD expectations, and we hope a next to leading order calculation will be available soon. The RMS deviation of the K_t kick caused by jet angular resolution in the CDF detector was simulated and is shown as the dashed line labelled 'Detector'.

To estimate the influence of QCD radiation on the measured K_t kick we devised a cut on additional jet activity which maintains an equal fraction of events in each bin of photon (and background) P_t. Requiring that all additional jets in the event have transverse momentum $P_{t,jet} < 0.28P_t + 6.6$ GeV is a 75% efficient cut, and the RMS deviation of the K_t kick for surviving events is shown with the asterisks in Fig 10b. Similarly, requiring that all additional jets satisfy $P_{t,jet} < 0.16P_t + 6.2$ GeV is 50% efficient and is shown by the triangles; requiring $P_{t,jet} < 0.09P_t + 5.0$ GeV is only 25%

efficient and is shown by the crosses. Note how the RMS deviation of the K_t kick decreases and becomes a flatter function of P_t as we tighten the cut on additional jet activity; this suggests we are removing events with QCD radiation, and that the P_t of the radiation may be correlated with the subprocess P_t. In any case, events with additional jet activity contribute significantly to the measured K_t kick.

5 Summary and Future Prospects

Preliminary results indicate that the inclusive direct photon cross section has an excess at low P_t compared to recent next to leading order QCD predictions. At $P_t > 20$ GeV the measured cross section agrees with QCD. The pseudorapidity of the leading jet, for both photons and background in the range $27 < P_t < 33$ GeV, is in good agreement with next to leading order QCD predictions. Measurements of the Kt kick in the combined photon-jet and pizero-jet final state have been made and hopefully a next to leading order calculation will be available soon.

Studies of the following topics related to photons have already begun or will soon begin: the inclusive cross section of events with two photons, the fragmentation of the leading jet in photon events, the search for $b' \to b\gamma$, the search for $W \to \pi\gamma$, and the cross section for $W\gamma$ production. All photon analysis topics will benefit from the planned installation of conversion detection chambers outside the CDF solenoid. The materials in the solenoid (1 radiation length) produce photon conversions, which will allow the new chambers to efficiently separate direct photons from background during the 1991 run.

Appendix A: CDF Collaborating Institutions

ANL - Brandeis - University of Chicago - Fermilab - INFN, Frascati - Harvard - University of Illinois - KEK - LBL - University of Pennsylvania - INFN, University of Scuola Normale Superiore of Pisa - Purdue - Rockefeller - Rutgers - Texas A&M - Tskuba - Tufts - University of Wisconsin

References

1. F. Abe et al., *Nucl. Inst. and Meth.* **A271**(1988)387.
2. L. Balka et al., *Nucl. Inst. and Meth.* **A267**(1988)272.
3. P. Aurenche, R. Baier and M. Fontannaz, FERMILAB-PUB-89/226-T(1989).
4. M. Diemoz, F. Ferroni, E. Longo and G. Martinelli, *Z. Phys.* **C39**(1988)21.
5. A. D. Martin, R. G. Roberts and W. J. Stirling, *Phys. Lett.* **B206**(1988)327.
6. S. Bhadra et al., *Nucl. Inst. and Meth.* **A268**(1988)92.
7. D. N. Brown, Ph.D. Thesis, Harvard University, 1989 (unpublished).
8. H. Baer, J. Ohnemus and J. F. Owens, FSU-HEP-900214(1990).